Inorganic Chemistry

Article

pubs.acs.org/IC

Synthesis, Crystal Structure, and Physical Properties of the Type-I Clathrate $Ba_{8-\delta}Ni_x\square_ySi_{46-x-y}$

U. Aydemir,* C. Candolfi, A. Ormeci, H. Borrmann, U. Burkhardt, Y. Oztan, N. Oeschler, M. Baitinger, F. Steglich, and Yu. Grin*

Max-Planck-Institut für Chemische Physik fester Stoffe, Nöthnitzer Straße 40, 01187 Dresden, Germany

Supporting Information

ABSTRACT: Type-I clathrate phase $Ba_8Ni_x\square_ySi_{46-x-y}$ ($\square$ = vacancy) was obtained from the elements at 1000 °C with the homogeneity range $2.4 \le x \le 3.8$ and $0 \le y \le 0.9$. In addition, samples with low Ni content (x = 1.4 and 1.6; y = 0) and small Ba deficiency were prepared from the melt by steel-quenching. Compositions were established by microprobe analysis and crystal structure determination. $Ba_{8-\delta}Ni_x\square_ySi_{46-x-y}$ crystallizes in the space group $Pm\bar{3}n$ (No. 223) with lattice parameter ranging from a = 10.3088(1) Å for $Ba_{7.9(1)}Ni_{1.4(1)}Si_{44.6(1)}$ to a = 10.2896(1) Å for $Ba_{8.00(3)}Ni_{3.82(4)}Si_{41.33(6)}$. Single-crystal X-ray diffraction data together with microprobe analysis indicate an increasing number of framework vacancies toward compositions with higher Ni content. For all compositions investigated, Ni K-edge X-ray absorption spectroscopy measurements showed an electronic state close to that of elemental Ni. All samples exhibit metallic-like behavior with moderate thermopower and low thermal conductivity in the temperature range 300−773 K. Samples with compositions $Ba_{7.9(1)}Ni_{1.4(1)}Si_{44.6(1)}$ and $Ba_{7.9(1)}Ni_{1.6(1)}Si_{44.4(1)}$ are superconducting with T_c values of 6.0 and 5.5 K, respectively.

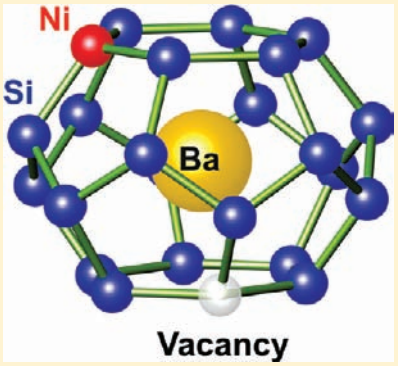

1. INTRODUCTION

The first type-I silicon clathrate, Na_8Si_{46}, was structurally characterized in 1965.[1] In the crystal structure, Si atoms form four-connected, covalently bonded framework with 20- and 24-atom polyhedral cages filled by Na atoms. Following the Zintl−Klemm concept, the valence electrons of Na are not needed to form the four-bonded silicon framework. Na_8Si_{46} shows metallic behavior,[2] which implies that the excess electrons occupy antibonding (conduction) bands according to $[Na^{1+}]_8[(4b)Si^0]_{46}\cdot 8e^-$. Later, it was shown that the polyhedral cages can also be filled by Ba atoms and clathrates can bear even larger amount of excess electrons as $Na_2Ba_6Si_{46}$ with $[Na^{1+}]_2[Ba^{2+}]_6[(4b)Si^0]_{46}\cdot 14e^-$.[3] This phase attracted considerable attention since it was found to be the first superconductor based on an sp^3-framework with $T_c \approx 4$ K.[4] A higher transition temperature of $T_c \approx 8$ K was found for Ba_8Si_{46}.[5] Ternary superconducting clathrates have been reported as well, in which silicon atoms are partially replaced with other elements, e.g., Ge,[6] Ga,[7] Cu,[8] Ag.[9] However, in all these cases, T_c was found to decrease with increasing content of substitution atoms, and superconductivity vanishes after a certain substitution level is reached. Generally, the number of excess electrons in clathrate-I silicides is reduced by the substitution atoms in the framework. In the Zintl phase $Ba_8Ga_{16}Si_{30}$, e.g., Si atoms are substituted by Ga resulting in the charge balance $[Ba^{2+}]_8[(4b)Ga^{1-}]_{16}[(4b)Si^0]_{30}$.[10−12] When full charge balance is achieved, semiconducting clathrates can be obtained. Such phases are of high interest for thermoelectric properties,[13−15] which depend on thermopower (α), electrical resistivity (ρ), and thermal conductivity (λ), and characterized by the dimensionless figure-of-merit, $ZT = (\alpha^2T)/(\rho\lambda)$. Intermetallic clathrates usually show favorably low lattice thermal conductivity regardless of composition. Hence, clathrates with high thermoelectric efficiency might be achieved by optimizing thermopower and electrical resistivity.[16] In this respect, clathrate systems with an extended homogeneity range are promising candidates, because they allow for tuning the charge carrier concentration through chemical composition. For example, clathrates in the systems Ba−Ni−Ge[17,18] and Ba−Au−Si[19,20] show either n- or p-type conduction behavior depending on the content of transition metal.

For the system Ba−Ni−Si, a clathrate-I phase was originally reported for only one composition $Ba_8Ni_{1.8}Si_{44.2}$.[21] Crystals of this composition were directly obtained from the melt, whereas the binary $Ba_{8-x}Si_{46}$ has been prepared only under high pressure[5,6,22,23] or, recently, by oxidation of $Li_2Ba_4Si_6$ with gaseous HCl.[24] Remarkably, the reported lattice parameter of $Ba_8Ni_{1.8}Si_{44.2}$ (a = 10.285(5) Å) is significantly smaller than that of Ba_8Si_{46} (a = 10.328(2) Å).[5]

Herein, more systematic studies were undertaken to determine the phase formation and the variations in the crystal structure with Ni content. We report on the phase stability, the homogeneity range and the crystal structure of the clathrate-I phase $Ba_{8-\delta}Ni_x\square_ySi_{46-x-y}$. X-ray absorption spectroscopy (XAS) measurements were carried out to elucidate the electronic state of Ni. We further demonstrate the possibility of achieving superconducting single-phase samples with lower

Received: December 24, 2011
Published: March 28, 2012

   dx.doi.org/10.1021/ic2027626 | Inorg. Chem. 2012, 51, 4730−4741

Table 1. Crystallographic Data for the Clathrate-I Phase Obtained at 1000 °C

composition (WDXS)	$Ba_{8.00(3)}Ni_{2.62(1)}Si_{42.57(3)}$	$Ba_{8.00(2)}Ni_{3.17(1)}Si_{43.03(2)}$	$Ba_{8.00(4)}Ni_{3.72(9)}Si_{41.83(5)}$
composition (refined)	$Ba_8Ni_{2.6}Si_{43.3}\square_{0.1}$	$Ba_8Ni_{3.2}Si_{42.4}\square_{0.4}$	$Ba_8Ni_{3.7}Si_{41.4}\square_{0.9}$
cryst syst; space group	cubic; $Pm\bar{3}n$ (No. 223)		
a (Å) (based on PXRD data)	10.2982(1)	10.2922(1)	10.2906(1)
no. of reflns (PXRD)	66	64	61
unit cell volume (Å^3)	1092.15(3)	1090.25(3)	1089.74(3)
Z; ρ_{calcd}(g cm^{-3})	1; 3.752	1; 3.776	1; 3.779
μ (mm^{-1})	4.90	5.01	5.14
F(000) (e)	1127	1131	1131
diffractometer	RIGAKU Spider		
λ (Å); monochromator	0.56087; multilayer-optics		
cryst size (μm^3)	20 × 35 × 55	10 × 10 × 40	20 × 30 × 50
T (K)	295		
θ range (deg)	3.82−34.97	3.12−30.11	3.12−30.65
indexes ranges	$-21 \le h \le 15$, $-16 \le k \le 12$, $-18 \le l \le 13$	$-3 \le h \le 15$, $-17 \le k \le 17$, $-17 \le l \le 18$	$-18 \le h \le 17$, $-18 \le k \le 15$, $-16 \le l \le 18$
absorption correction	multiscan		
no. of reflns collected; unique; unique [$I > 4\sigma(I)$]	12994; 909 [R_{int} =0 0.04]; 720	7263; 717 [R_{int} =0 0.03]; 503	13319; 651 [R_{int} = 0.03]; 561
refined params	25	33	36
refinement method	full-matrix least-squares on F		
$R(F)$; $wR(F^2)$ [$I > 4\sigma(I)$]	0.030; 0.052	0.023; 0.039	0.021; 0.035

dx.doi.org/10.1021/ic2027626 | Inorg. Chem. 2012, 51, 4730−4741

Table 2. Atomic Coordinates, Displacement Parameters (in Å^2), and Site Occupancies for $Ba_8Ni_{2.6}Si_{43.3}\square_{0.1}$ (top), $Ba_8Ni_{3.2}Si_{42.4}\square_{0.4}$ (middle), and $Ba_8Ni_{3.7}Si_{41.4}\square_{0.9}$ (bottom)

atom	site	x	y	z	U_{eq}[a]	Occ.
Ba1	2*a*	0	0	0	0.00949(5)	1
Ba2	24*k*	0.2474(8)	0.5163(3)	0	0.0159(5)	0.25
Ni1/Si1	6*c*	1/4	0	1/2	0.0086(2)	0.433/0.55(1)
Si2	16*i*	0.18461(6)	x	x	0.00814(8)	1
Si31	24*k*	0	0.3087(2)	0.1164(2)	0.0089(3)	0.567(4)
Si32	24*k*	0	0.3148(2)	0.1279(2)	0.0097(4)	0.433

atom	U_{11}	U_{22}	U_{33}	U_{12}	U_{13}	U_{23}
Ba1	0.00949(8)	U_{11}	U_{11}	0	0	0
Ba2	0.0122(5)	0.0145(6)	0.0211(10)	0.0040(6)	0	0
Ni1/Si1	0.0097(4)	0.0080(3)	U_{22}	0	0	0
Si2	0.0081(1)	U_{11}	U_{11}	−0.0008(1)	U_{12}	U_{12}
Si31	0.0095(5)	0.0068(5)	0.0106(5)	0	0	0.0012(4)
Si32	0.0066(6)	0.0128(7)	0.0098(7)	0	0	0.0020(6)

atom	site	x	y	z	U_{eq}[a]	Occ.
Ba1	2*a*	0	0	0	0.00899(5)	1
Ba2	24*k*	0.24105(7)	0.51441(7)	0	0.0151(5)	0.25
Ni1/Si1	6*c*	1/4	0	1/2	0.0073(2)	0.533/0.404(7)
Si2	16*i*	0.18434(5)	x	x	0.00796(8)	1
Si31	24*k*	0	0.3067(2)	0.1122(2)	0.0063(4)	0.405(3)
Si32	24*k*	0	0.3151(2)	0.1281(2)	0.0074(3)	0.533
Si33	24*k*	0	0.3278(13)	0.1325(13)	0.009(2)[b]	0.063(3)

atom	U_{11}	U_{22}	U_{33}	U_{12}	U_{13}	U_{23}
Ba1	0.00899(9)	U_{11}	U_{11}	0	0	0
Ba2	0.0019(2)	0.0188(10)	0.0315(10)	0.0027(5)	0	0
Ni1/Si1	0.0079(5)	0.0069(3)	U_{22}	0	0	0
Si2	0.0080(1)	U_{11}	U_{11}	−0.0006(2)	U_{12}	U_{12}
Si31	0.0082(7)	0.0069(7)	0.0037(7)	0	0	−0.0025(6)
Si32	0.0073(5)	0.0066(5)	0.0082(5)	0	0	−0.0001(4)

atom	site	x	y	z	U_{eq}[a]	Occ.
Ba1	2*a*	0	0	0	0.01052(5)	1
Ba2	24*k*	0.24311(9)	0.51155(9)	0	0.0214(8)	0.25
Ni1/Si1	6*c*	1/4	0	1/2	0.0088(2)	0.617/0.231(8)
Si2	16*i*	0.18434(5)	x	x	0.00981(7)	1
Si31	24*k*	0	0.3072(3)	0.1094(3)	0.0076(6)	0.232(3)
Si32	24*k*	0	0.3122(1)	0.1231(1)	0.0099(3)	0.617
Si33	24*k*	0	0.3216(5)	0.1343(5)	0.0080(9)	0.152(4)

atom	U_{11}	U_{22}	U_{33}	U_{12}	U_{13}	U_{23}
Ba1	0.01052(8)	U_{11}	U_{11}	0	0	0
Ba2	0.0085(2)	0.019(2)	0.037(2)	−0.0008(7)	0	0
Ni1/Si1	0.0090(3)	0.0082(2)	U_{22}	0	0	0
Si2	0.0098(1)	U_{11}	U_{11}	−0.0006(1)	U_{12}	U_{12}
Si31	0.0048(9)	0.0095(11)	0.0086(10)	0	0	−0.0006(8)
Si32	0.0119(4)	0.0089(4)	0.0089(4)	0	0	0.0016(3)
Si33	0.0040(2)	0.008(2)	0.012(2)	0	0	−0.0027(14)

[a] U_{eq} is defined as one-third of the trace of the orthogonalized U_{ij} tensor, which is exp $(-2\pi^2\,[h^2a^{*2}U_{11} + \ldots + 2\,h\,k\,a^*b^*U_{12}])$. [b] Refined in isotropic approximation (U_{iso})

Ni content. Finally, we investigated the thermoelectric efficiency of the clathrate phase at high temperatures. A thorough theoretical and experimental investigation of the electronic band structure and the low-temperature transport properties was already reported elsewhere.[25]

2. EXPERIMENTAL SECTION

2.1. Synthesis. Polycrystalline samples were synthesized by reaction of crystalline Ba (ChemPur, 99.9% metals basis), Ni powder (ChemPur, 99.9% metals basis) and ground Si pieces (ChemPur, 99.9999% metals basis) in an argon-filled glovebox. Stoichiometric amounts of elements with total weight of around 2 g were placed in an open glassy carbon crucible (⌀ = 12 mm, l = 12 mm, Sigradur G, HTW) and slowly heated to the melt using an induction furnace (5 kW, coil ⌀ = 40 mm, l = 35 mm, Hüttinger; IR pyrometer, Maurer). The melts were then cooled down to room temperature by pouring on a steel plate. The resulting specimens were characterized by metallography and powder X-ray diffraction (PXRD). For the annealing, specimens were placed in glassy carbon crucibles and welded in tantalum ampules which were in turn sealed in an argon-filled quartz tube. To avoid any influence from the cooling process, we quenched the ampules in water. Clathrate phase was obtained after 1 week of annealing at 1000 °C. Superconducting samples $Ba_{8-\delta}Ni_xSi_{46-x}$ ($\delta \approx 0.1$; x = 1.4 and 1.6) with low Ni content were obtained by fast cooling of the melt between two steel plates (steel-

dx.doi.org/10.1021/ic2027626 | Inorg. Chem. 2012, 51, 4730−4741

quenching).[26] Besides the clathrate phase, the reaction products mainly contained $BaSi_2$ and α-Si, which were removed by treatment with 3 M HCl for 8 h and afterward by 1 M NaOH for 8 h (see Figure S1 in the Supporting Information).

2.2. Powder X-ray Diffraction. PXRD data were obtained using an X-ray Guinier diffraction technique (Huber G670 camera, Cu-$K\alpha_1$ radiation, λ = 1.54056 Å, graphite monochromator, $5° \leq 2\theta \leq 100°$, $\Delta 2\theta = 0.005°$). The reflection positions were determined by profile deconvolution and corrected by LaB_6 (a = 4.15683(9) Å at 295(2) K) as internal standard. The unit cell parameters were calculated from least-squares refinement and the Rietveld refinements were performed by using WinCSD program package.[27]

2.3. Single-Crystal X-ray Diffraction. Room-temperature single-crystal X-ray data were collected with a rotating-anode diffractometer (RIGAKU Spider, Varimax optical system, Ag-$K\alpha$ radiation, λ = 0.56087 Å). A multiscan absorption correction was applied during the data collection. Crystal structure determination and refinement were carried out with WinCSD software. Details regarding the data collection and structure refinement are given in Table 1, atomic coordinates and displacement parameters are listed in Table 2.

2.4. Microstructure Analysis. Samples stable to air and moisture were embedded in epoxy resin substrate containing carbon fibers. Grinding was performed with silicon carbide abrasive discs together with alcohol including lubricants. Polishing was achieved in steps by using different polishing discs of micrometer-sized diamond powders (6, 3, 0.25 μm) in paraffin. Air or moisture sensitive samples were polished in an Ar-filled glovebox using hexane as lubricant. Optical microscopy images were obtained by a polarization microscope (Zeiss Axioplan). Phase identification was carried out by using a Philips XL 30 scanning electron microscope (SEM) with integrated energy dispersive X-ray (EDX) spectrometer. The composition of the clathrate phase was determined with a Cameca SX 100 wavelength dispersive X-ray (WDX) spectrometer using Ba_6Ge_{25} and NiSi as standards for the determination of Ba, Ni, and Si concentrations.

2.5. X-ray Absorption Spectroscopy. X-ray absorption near-edge structure (XANES) and the extended X-ray absorption fine structure (EXAFS) were studied in the spectral region of the Ni K-edge (8333 eV). The spectra were recorded in transmission mode at the EXAFS beamline C of HASYLAB at German Electron Synchrotron (DESY). Further experimental details are given in the Supporting Information (section S.1).

2.6. Thermal Analysis. Thermal behavior of the samples was investigated with a Netzsch DSC 404C instrument. Bulk pieces of about 30 mg were transferred to a glassy carbon crucible (⌀ = 4 mm, l = 6 mm, Sigradur G, HTW) which was then sealed in an Nb crucible (⌀ = 5 mm, 600 mg). The system was heated under Ar atmosphere from room temperature up to 1300 °C applying different heating rates of 2−10 °C/min.

2.7. Calculation Procedures. First-principles electronic structure calculations within the local density approximation to the density functional theory were performed using the all-electron, full-potential local orbital method (FPLO).[28] Perdew−Wang parametrization of the exchange-correlation potential was employed.[29] The calculations for $Ba_8Ni_x\square_ySi_{46-x-y}$ were performed on models with the compositions (x = 0−4, 6; y = 0) and (x = 3, 4; y = 1). To compute heats of formation and assess the stability of the clathrate phase, total energy calculations for the elemental solids (bcc Ba,[30] ferromagnetic fcc Ni,[30] and α-Si[30]), $BaSi_2$,[31] NiSi,[32] and $NiSi_2$[33] were carried out on fully optimized crystal structures. In regard to the clathrates, however, only the end-members (x = 0 and 6; y = 0) were fully optimized, whereas for the other compositions experimentally determined values of the structural parameters were used. In the crystal structure (space group $Pm\bar{3}n$), Ni and Si atoms as well as vacancies share the 6c position as discussed in crystal structure part (see section 3.5). For the calculations, partial occupancies were modeled by using supercells which were constructed according to the group−subgroup relations. The details regarding this matter were explained in a recent publication.[25]

2.8. Physical Properties. For the measurements, specimens with the required shape were cut from annealed ingots by using a diamond-wire saw. Electrical resistivity and thermopower were measured simultaneously in the temperature range 300−773 K using a commercial setup (ZEM-3, Ulvac-Riko) on prism-shaped specimens of 2 × 2 × 6 mm^3. Thermal diffusivity a was measured from 300 to 773 K using a Netzsch LFA 427 apparatus on specimens with 6 × 6 × 1 mm^3. The thermal conductivity was then calculated via $\lambda = aC_p\rho_v$ where C_p is the specific heat and ρ_v is the density. The specific heat was considered to be constant and equal to the Dulong-Petit value throughout the temperature range investigated. No correction for thermal dilatation was applied.

The superconductivity of the clathrate phase with low Ni concentrations was characterized by electrical resistivity measurements in the temperature range 2−10 K, using the AC option of a physical property measurements system (PPMS, Quantum Design). Copper wires were used as contacts and attached to the samples using a tiny amount of silver paint. The measurements were performed on prism-shaped specimens with the size of 1.5 × 1 × 6.7 mm^3 which were hot-pressed at 300 °C under 0.5 GPa pressure.

3. RESULTS AND DISCUSSION

3.1. Isothermal Section of the System $BaSi_2$−NiSi−α-Si at 1000 °C. Homogeneous samples of the clathrate-I phase $Ba_8Ni_x\square_ySi_{46-x-y}$ were obtained for $2.4 \leq x \leq 3.8$ and $y \leq 0.9$ after annealing at 1000 °C for 1 week. The phase equilibria of the clathrate phase at this temperature are shown in Figure 1. The three-phase region between clathrate-I + $BaSi_2$ + α-Si is observed in the samples with the nominal compositions $Ba_8Ni_{0.5}Si_{45.5}$ (Figure 1a, sample 1), $Ba_8Ni_2Si_{44}$ (Figure 1a, sample 2), $Ba_{22.5}Ni_{2.5}Si_{75}$ (Figure 1a, sample 3), and $Ba_{10}Ni_2Si_{88}$ (Figure 1a, sample 4). The microstructure of these samples always showed well separated grains of $BaSi_2$, α-Si and clathrate-I phase (C-I) in the respective amounts (Figure 2a and Figure S2a-c in the Supporting Information). The lower limit of Ni content in the homogeneity range $Ba_8Ni_x\square_ySi_{46-x-y}$ at 1000 °C was determined to be $Ba_{8.00(5)}Ni_{2.36(4)}Si_{43.94(6)}$ from the sample 2 (Table 3). Two-phase regions were found at the compositions $Ba_{18}Ni_5Si_{77}$ (Figure 1a, sample 5), containing $BaSi_2$ and clathrate (Figure 2b), and $Ba_{13}Ni_5Si_{82}$ (Figure 1a, sample 6) showing a mixture of α-Si and clathrate (Figure 2c). Samples with the composition $Ba_{25}Ni_5Si_{70}$ (Figure 1a, sample 7) and $Ba_{2.5}Ni_{2.5}Si_{95}$ (Figure 1a, sample 8) belong to three-phase regions $BaSi_2$ + clathrate-I + melt and clathrate-I + α-Si + melt, respectively (see Figure S2d, e in the Supporting Information). For the composition $Ba_8Ni_4Si_{42}$ (Figure 1a, sample 9), the clathrate phase is in equilibrium with the melt. The microstructure of this sample shows large grains of the clathrate phase surrounded by a finely grained mixture formed from the melt after the sample was quenched from 1000 °C to room temperature (Figure 2d). The composition $Ba_{8.00(3)}Ni_{3.82(4)}Si_{41.33(6)}$ determined for the clathrate phase in this sample represents the upper limit of Ni content at 1000 °C, which was also confirmed from samples with higher nominal Ni content (Table 3). Analysis of the clathrate-I phase by wavelength dispersive X-ray spectroscopy (WDXS) shows a distinct deviation from the nominal composition $Ba_8Ni_xSi_{46-x}$ (Figure 1b, Table 3). In particular for higher Ni contents, the ratio of concentrations $(c_{Ni} + c_{Si})/c_{Ba}$ is influenced by the presence of vacancies in the Ni−Si framework. Full occupancy of the Ba sites as well as the existence of framework vacancies were shown by structure analyses based on single crystal data (see section 3.5).

Clathrate products obtained at 1000 °C were investigated by thermal analysis. For all compositions $2.4 < x < 3.8$, the peritectic decomposition of the clathrate-I phase was indicated by a single, strong endothermic effect close to T = 1105 °C,

dx.doi.org/10.1021/ic2027626 | Inorg. Chem. 2012, 51, 4730−4741

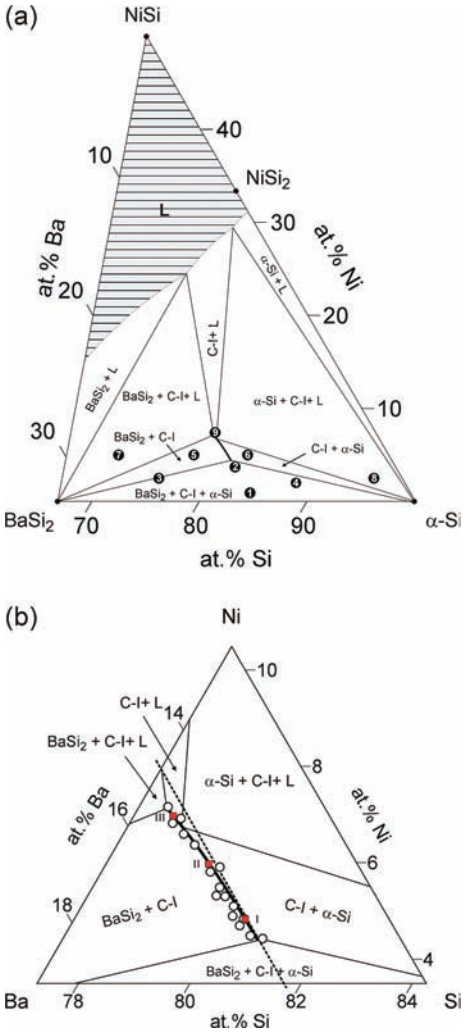

Figure 1. (a) Isothermal section of the system $BaSi_2$–NiSi–α-Si at 1000 °C based on the investigated samples $Ba_8Ni_{0.5}Si_{45.5}$ (**1**), $Ba_8Ni_2Si_{44}$ (**2**), $Ba_{22.5}Ni_{2.5}Si_{75}$ (**3**), $Ba_{10}Ni_2Si_{88}$ (**4**), $Ba_{18}Ni_5Si_{77}$ (**5**), $Ba_{13}Ni_5Si_{82}$ (**6**), $Ba_{25}Ni_5Si_{70}$ (**7**), $Ba_{2.5}Ni_{2.5}Si_{95}$ (**8**), and $Ba_8Ni_4Si_{42}$ (**9**). The part of the phase diagram, which should be liquid at 1000 °C is only estimated and shown as hatched gray area. (**b**) The homogeneity range of the clathrate phase based on the WDXS data is shown as thick line. The refined single crystal compositions (**I**, **II**, **III**) are shown with squares. The dashed-line represents the isoconcentrate of 14.81 at % Ba ($Ba_8Ni_xSi_{46-x}$).

followed by a broad endothermic peak indicating the liquidus (see Figure S3 in the Supporting Information). On cooling, several exothermic effects appeared in agreement with the incongruent (peritectic) formation of the clathrate phase.

3.2. Estimation of Primary Crystallization Field of the Clathrate-I Phase. The type-I clathrate $Ba_8Ni_x\square_ySi_{46-x-y}$ is the only known ternary phase in the composition triangle $BaSi_2$–NiSi–α-Si.[21,25] For the binary systems $BaSi_2$–Si and NiSi–Si, a eutectic composition was reported at 77 at % Si (Figure 3, point ε_1),[34] and at 56 at % Si (point ε_2),[35] respectively. The eutectic point ε_3 of the quasi-binary system $BaSi_2$–NiSi was assigned from sample 1 to be 20 at % Ba, 20 at % Ni, 60 at % Si with a melting temperature at around 920 °C (see Figure S4 in the Supporting Information). At this composition, the microstructure contains finely distributed crystallites of $BaSi_2$ and NiSi (Figure 4a). The ternary eutectic point of $BaSi_2$, NiSi and the clathrate phase was roughly

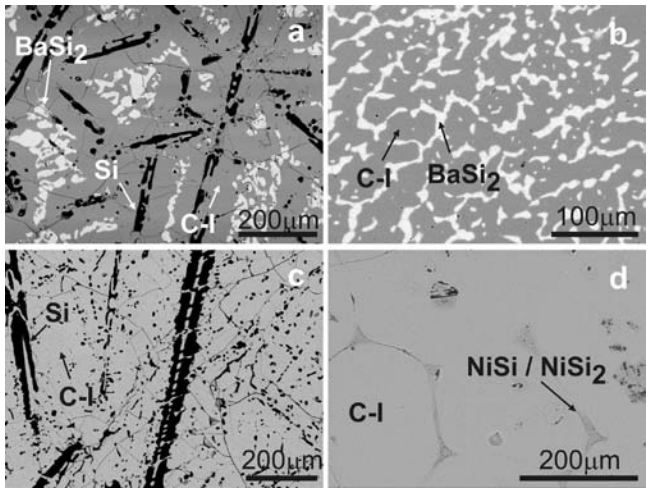

Figure 2. Microstructure (SEM, BSE contrast) of samples in the system $BaSi_2$–NiSi–α-Si after annealing at 1000 °C: (a) $Ba_8Ni_2Si_{44}$ (sample 2), (b) $Ba_{18}Ni_5Si_{77}$ (sample 5), (c) $Ba_{13}Ni_5Si_{82}$ (sample 6), and (d) $Ba_8Ni_4Si_{42}$ (sample 9). Sample numbers are given according to Figure 1 and observed phases are marked.

estimated by microstructure analysis of samples 2 (Figure 4b) and 3 (Figure 4c) to be 8 at % Ba, 34 at % Ni, 58 at % Si (Figure 3, point τ).

The primary crystallization field of α-Si is subdivided into three parts. At low Ni content, it is in contact with the primary crystallization field of $BaSi_2$. Microstructure analysis of sample 4 (Figure 4d) showed large and well-shaped crystallites of the primary phase α-Si. On further cooling, smaller but distinctly shaped crystallites of $BaSi_2$ and α-Si appear. With increasing Ni content, the peritectic reaction L + α-Si → C–I is observed at 1105 °C. Hence, the microstructure of samples 5–7 contains grains of α-Si, enveloped by the crystallites of the clathrate-I, and remaining $BaSi_2$ (sample 7, Figure 4e). Further increase of Ni content leads to formation of the clathrate-I phase besides α-Si. The microstructure of sample 8 (Figure 4f) and sample 9 (Figure 4g) contains primary grains of α-Si that are almost entirely enveloped by $NiSi_2$ crystallites. Upon crystallization of $NiSi_2$, the crystallization field of the clathrate phase is reached as both phases are formed with well-shaped crystals. At lower temperatures, the eutectic channel between clathrate and NiSi is reached, represented in the microstructure by areas with a finely grained mixture of NiSi and the clathrate phase. The primary crystallization field of $BaSi_2$ is observed in the samples 10 and 2 in which primary grains of $BaSi_2$ are in contact with clathrate-I (Figure 4h) or NiSi crystallites (Figure 4b), respectively. The primary crystallization of NiSi is observed in sample 3 (primary grains of NiSi in contact with $BaSi_2$ crystallites, Figure 4c). The small field of crystallization of $NiSi_2$ may be expected close to the binary system α-Si–NiSi and was not further characterized. The primary crystallization of the clathrate-I phase is observed for the samples 11–14 (region C-I, Figure 3) showing large areas of clathrate-I phase in contact with $BaSi_2$ and NiSi (samples 11–13, Figure 4i) or NiSi and $NiSi_2$ (sample 14), respectively. Almost equal amounts of clathrate-I and $BaSi_2$ phases are observed in sample 13 (Figure 4j) suggesting that the eutectic channel is running close to this concentration point.

3.3. Metastable Compositions. The clathrate phase with distinctly lower Ni content was obtained by steel-quenching of molten samples. The compositions were determined from

dx.doi.org/10.1021/ic2027626 | Inorg. Chem. 2012, 51, 4730–4741

Table 3. Lattice Parameter and Composition of the Clathrate Phase (C−I) in the Samples Annealed at 1000 °C for 1 Week

nominal composition	products (PXRD & EDXS)	composition (WDXS)	a (Å)
$Ba_8Ni_{0.2}Si_{45.8}$	C-I (<10%), $BaSi_2$ (>40%), α-Si (>50%)	$Ba_{8.0(3)}Ni_{2.5(1)}Si_{42.0(2)}$	10.2994(1)
$Ba_8Ni_{0.5}Si_{45.5}$	C-I (<20%), $BaSi_2$ (>40%), α-Si (>40%)	$Ba_{8.0(3)}Ni_{2.5(1)}Si_{42.3(3)}$	10.2997(1)
$Ba_8Ni_1Si_{45}$	C-I (>40%), $BaSi_2$ (<30%), α-Si (<30%)	$Ba_{8.00(3)}Ni_{2.43(2)}Si_{43.30(4)}$	10.3007(1)
$Ba_8Ni_2Si_{44}$	C-I (>80%), $BaSi_2$ (<10%), α-Si (<10%)	$Ba_{8.00(5)}Ni_{2.36(4)}Si_{43.94(6)}$	10.3011(2)
$Ba_8Ni_2Si_{44}$	C-I (>80%), $BaSi_2$ (<10%), α-Si (<10%)	$Ba_{8.00(3)}Ni_{2.44(2)}Si_{42.81(3)}$	10.3007(1)
$Ba_8Ni_{2.5}Si_{43.5}$	C−I (>95%), $BaSi_2$ (<3%), α-Si (<2%)	$Ba_{8.00(3)}Ni_{2.62(1)}Si_{42.57(3)}$	10.2982(1)
$Ba_8Ni_{2.5}Si_{43.5}$	C-I (>95%), $BaSi_2$ (<3%), α-Si (<2%)	$Ba_{8.00(2)}Ni_{2.64(2)}Si_{43.23(4)}$	10.2981(1)
$Ba_8Ni_{2.65}Si_{43.35}$	C-I (>96%), $BaSi_2$ (<2%), α-Si (<2%)	$Ba_{8.00(5)}Ni_{2.73(1)}Si_{42.89(5)}$	10.2958(1)
$Ba_8Ni_{2.75}Si_{43.25}$	C-I (>98%), $BaSi_2$ (<1%), α-Si (<1%)	$Ba_{8.00(2)}Ni_{2.81(2)}Si_{42.10(3)}$	10.2951(1)
$Ba_8Ni_{2.75}Si_{43.25}$	C-I (>98%), $BaSi_2$ (<1%), α-Si (<1%)	$Ba_{8.00(2)}Ni_{2.83(1)}Si_{42.61(1)}$	10.2947(1)
$Ba_8Ni_{2.85}Si_{43.15}$	C-I (>98%), $BaSi_2$ (<1%), α-Si (<1%)	$Ba_{8.00(1)}Ni_{2.93(1)}Si_{42.50(1)}$	10.2929(1)
$Ba_8Ni_3Si_{43}$	C-I (>98%), $BaSi_2$ (<1%), α-Si (<1%)	$Ba_{8.00(2)}Ni_{3.11(1)}Si_{42.26(2)}$	10.2923(1)
$Ba_8Ni_3Si_{43}$	C-I (>98%), $BaSi_2$ (<1%), α-Si (<1%)	$Ba_{8.00(2)}Ni_{3.17(1)}Si_{43.03(2)}$	10.2922(1)
$Ba_8Ni_{3.5}Si_{42.5}$	C-I (>99%), α-Si (<1%)	$Ba_{8.00(7)}Ni_{3.42(3)}Si_{41.99(4)}$	10.2904(1)
$Ba_8Ni_{3.5}Si_{42.5}$	C-I (>99%), NiSi (<1%)	$Ba_{8.00(3)}Ni_{3.46(4)}Si_{41.56(7)}$	10.2897(1)
$Ba_8Ni_4Si_{42}$	C-I (>98%), $BaSi_2$, NiSi, $NiSi_2$ (<2%)	$Ba_{8.00(4)}Ni_{3.72(9)}Si_{41.83(5)}$	10.2906(1)
$Ba_8Ni_4Si_{42}$	C-I (>98%), $BaSi_2$, NiSi, $NiSi_2$ (<2%)	$Ba_{8.00(3)}Ni_{3.82(4)}Si_{41.33(6)}$	10.2896(1)
$Ba_8Ni_6Si_{40}$	C-I (>90%), $BaSi_2$, NiSi, $NiSi_2$ (<5%)	$Ba_{8.00(1)}Ni_{3.62(3)}Si_{41.16(3)}$	10.2907(1)

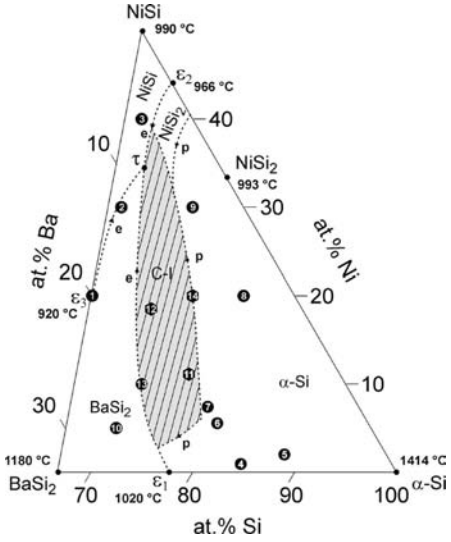

Figure 3. Estimated primary crystallization fields in the system $BaSi_2$−NiSi−α-Si. The investigated compositions are numbered as $Ba_{20}Ni_{20}Si_{60}$ (**1**), $Ba_{12}Ni_{30}Si_{58}$ (**2**), $Ba_5Ni_{40}Si_{55}$ (**3**), $Ba_8Ni_{0.5}Si_{45.5}$ (**4**), $Ba_{10}Ni_2Si_{88}$ (**5**), $Ba_8Ni_3Si_{43}$ (**6**), $Ba_8Ni_4Si_{42}$ (**7**), $Ba_5Ni_{20}Si_{75}$ (**8**), $Ba_5Ni_{30}Si_{65}$ (**9**), $Ba_{25}Ni_5Si_{70}$ (**10**), $Ba_8Ni_6Si_{40}$ (**11**), $Ba_8Ni_{10}Si_{36}$ (**12**), $Ba_{20}Ni_{10}Si_{70}$ (**13**), and $Ba_{10}Ni_{20}Si_{70}$ (**14**). Binary and ternary eutectics are marked with ε and τ, respectively.

Rietveld refinement on PXRD data and qualitatively confirmed by EDXS on pressed-powder after removing $BaSi_2$ and α-Si with dilute HCl and NaOH (Table 4 and Table S4 in the Supporting Information). From the starting composition $Ba_8Ni_{0.2}Si_{45.8}$, a clathrate phase with the composition $Ba_{7.9(1)}Ni_{1.4(1)}Si_{44.6(1)}$ (a = 10.3088(1) Å) was formed as a minority product together with $BaSi_2$ and α-Si. Similarly, $Ba_{7.9(1)}Ni_{1.6(1)}Si_{44.4(1)}$ (a = 10.3078(1) Å) was obtained starting from $Ba_8Ni_{0.5}Si_{45.5}$. In the DSC experiment, single phase $Ba_{7.9(1)}Ni_{1.6(1)}Si_{44.4(1)}$ showed an exothermic effect at ∼715 °C on heating with 10 K/min indicating the decomposition of a metastable phase (see Figure S5 in the Supporting Information). Therefore, it is possible that the steel-quenched clathrate products with low Ni content belong to a Ni-stabilized high-pressure phase $Ba_{8-\delta}Ni_xSi_{46-x}$.

3.4. Heat of Formation and Phase Stability. The phase stability of clathrates can be estimated by comparison of the ground-state energies.[36,37] The heat of formation of $Ba_8Ni_x\square_ySi_{46-x-y}$ was computed on the basis of the total energies obtained from first principles electronic structure calculations by considering the following balance

$$8Ba_{bcc} + xNi_{fcc;FM} + (46 - x - y)\alpha\text{-Si} = Ba_8Ni_x\square_ySi_{46-x-y} + \Delta H_f(x, y) \quad (1)$$

The stability of the clathrate phase with respect to the competing phases $BaSi_2$, NiSi, $NiSi_2$, and α-Si was also explored (see Table 5). Since both NiSi and $NiSi_2$ can form by decomposition of the clathrate phase, we took into account the two limiting balances:

$$Ba_8\square_xNi_x\square_ySi_{46-x-y} = 8BaSi_2 + xNiSi + (30 - 2x - y)\alpha\text{-Si} + \Delta E_1(x, y) \quad (2a)$$

$$Ba_8Ni_x\square_ySi_{46-x-y} = 8BaSi_2 + xNiSi_2 + (30 - 3x - y)\alpha\text{-Si} + \Delta E_2(x, y) \quad (2b)$$

In agreement with the phase diagram, eq 2b is more realistic because $NiSi_2$ was calculated to be more stable than NiSi + α-Si by 46.6 meV/atom.

The heat of formation ΔH_f of $Ba_8Ni_x\square_ySi_{46-x-y}$ (for y = 0) varies linearly with Ni content with two different slopes in the ranges $0 \le x \le 3$ and $3 \le x \le 6$ (Figure 5 inset). The additional energy saved upon forming a clathrate with one more Ni atom per formula unit for x up to 3 is almost twice that for $x > 3$. In this context, it is remarkable that the composition with x = 3 was also found to be special as it delineates two regions of different transport behavior.[25] Examination of Table 5 and Figure 5 reveals that: (i) all clathrates with compositions $x \le 4$ are stable according to eq 2a; (ii) the binary clathrate Ba_8Si_{46} and the compositions with $1 < x < 4$ are stable according to eq 2b; (iii) the composition with x = 3 is the most stable one; and (iv) compositions with vacancies (y = 0) are unstable. ΔE_1 and

dx.doi.org/10.1021/ic2027626 | Inorg. Chem. 2012, 51, 4730−4741

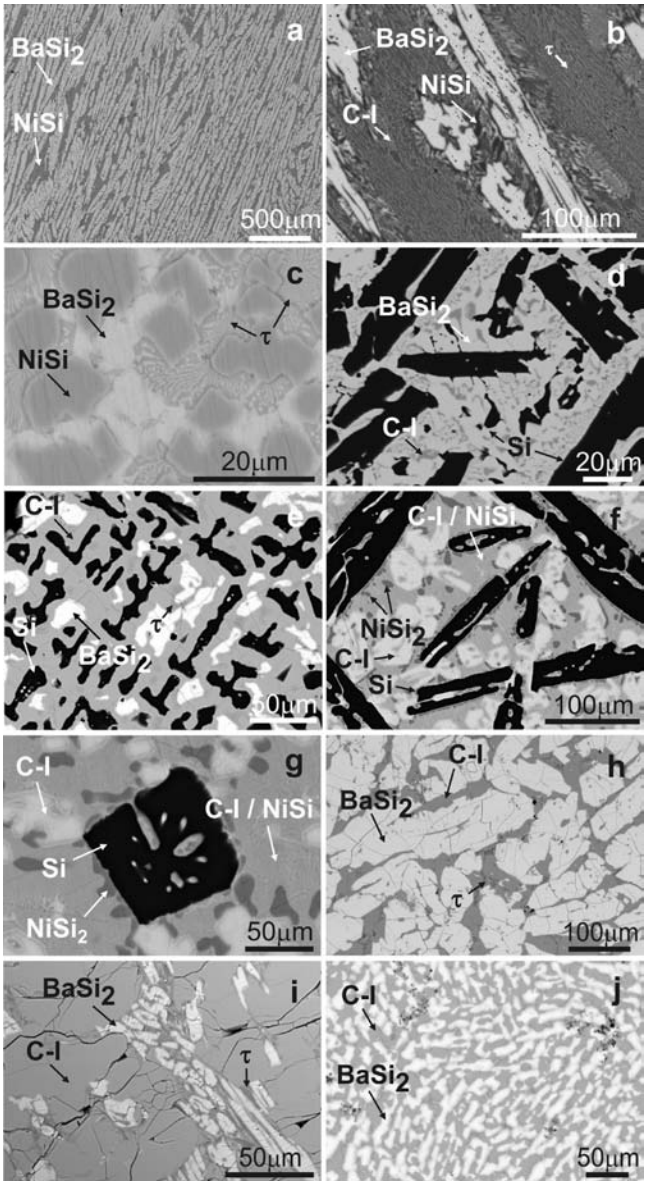

Figure 4. SEM images (BSE contrast) of the samples obtained by fast cooling from the melt in the system $BaSi_2$–NiSi–α-Si. The nominal compositions of the samples are: (a) $Ba_{20}Ni_{20}Si_{60}$ (sample 1), (b) $Ba_{12}Ni_{30}Si_{58}$ (sample 2), (c) $Ba_5Ni_{40}Si_{55}$ (sample 3), (d) $Ba_8Ni_{0.5}Si_{45.5}$ (sample 4), (e) $Ba_8Ni_4Si_{42}$ (sample 7), (f) $Ba_5Ni_{20}Si_{75}$ (sample 8), (g) $Ba_5Ni_{30}Si_{65}$ (sample 9), (h) $Ba_{25}Ni_5Si_{70}$ (sample 10), (i) $Ba_8Ni_6Si_{40}$ (sample 11), and (j) $Ba_{20}Ni_{10}Si_{70}$ (sample 13). Sample numbers are given according to Figure 3 and observed phases are marked.

Table 4. Lattice Parameter and Composition of the Clathrate Phase (C–I) in the Samples Obtained by Steel-Quenching

nominal composition	products (PXRD & EDXS)	composition (EDXS)	a (Å)
$Ba_8Ni_{0.2}Si_{45.8}$	C-I (<5%), $BaSi_2$ (>40%), α-Si (>50%)	$Ba_{7.5}Ni_{1.6}Si_{44.4}$	10.3088(1)
$Ba_8Ni_{0.5}Si_{45.5}$	C-I (<10%), $BaSi_2$ (>40%), α-Si (>40%)	$Ba_{7.5}Ni_{1.8}Si_{44.2}$	10.3078(1)
$Ba_8Ni_3Si_{43}$	C-I (>60%), $BaSi_2$ (<20%), α-Si (<20%)	$Ba_8Ni_{3.0}Si_{45.6}$	10.2932(1)
$Ba_8Ni_{3.5}Si_{42.5}$	C-I (>70%), $BaSi_2$ (<15%), α-Si (<15%)	$Ba_8Ni_{3.0}Si_{42.3}$	10.2927(1)
$Ba_8Ni_6Si_{40}$	C-I (>80%), $BaSi_2$ (<15%), NiSi(<5%)	$Ba_8Ni_{3.2}Si_{45.9}$	10.2935(1)

Table 5. ΔH_f (eq 1), ΔE_1 (eq 2a), and ΔE_2 (eq 2b) in meV atom^{-1} for $Ba_8Ni_x\square_ySi_{46-x-y}$[a]

(x, y)	ΔH_f	ΔE_1	ΔE_2
(0, 0)	171.3	−1.8	−1.8
(1, 0)	193.3	−2.2	0.4
(2, 0)	218.2	−5.6	−0.4
(3, 0)	243.9	−9.7	−1.9
(3, 1)	222.0	16.6	24.6
(4, 0)	257.0	−1.2	9.2
(4, 1)	231.3	29.4	39.9
(6, 0)	285.8	13.1	28.2

[a]Negative values of ΔE indicate that the clathrate phase is more stable than the competing phases.

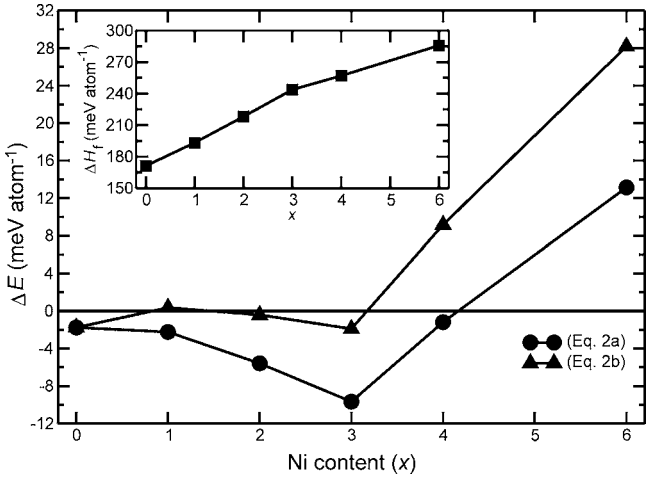

Figure 5. Enthalpies ΔE_1 (●), ΔE_2 (▲), and heat of formation (inset) as a function of nominal Ni content for vacancy-free compositions.

ΔE_2 having different signs for cases $x = 1$ and $x = 4$ should be considered taking two aspects into account: the ratio of the balances in eqs 2a and 2b is indeterminant and none of the clathrate models was optimized in a supercell. Although both aspects may be important for the $x = 1$ case, only the former is crucial for the $x = 4$ case. Furthermore, the presence of vacancies at the 6*c* site and the associated entropy contributions of phonons to the free energy introduce more uncertainty to the case of $x = 4$. Since after three Ni atoms, addition of an extra Ni atom saves less energy, the competing phases quickly become more favorable for $x > 3$. This result reflects a tendency to avoid two Ni atoms to be situated at consecutive 6*c* positions of the same six-ring, which leads to increased bond distances between the atoms at the 24*k* sites. Finally, $Ba_8Ni_6Si_{40}$ ($x = 6$) is found to be unstable in agreement with the fact that clathrate-I at this composition has not been observed yet.

The effect of vacancy formation on phase stability of clathrates was investigated for compositions with $x = 3$ and 4 using the following balances:

$$Ba_8Ni_3Si_{43} = Ba_8Ni_3Si_{42}\square_1 + \alpha\text{-Si} + \Delta E_v \quad (3a)$$

$$Ba_8Ni_4Si_{42} = Ba_8Ni_4Si_{41}\square_1 + \alpha\text{-Si} + \Delta E_v \quad (3b)$$

The computed vacancy formation energies are −1.4 and −1.6 eV for one vacancy per formula unit for $x = 3$ and 4, respectively, leading to the conclusion that internal energy contributions alone would favor vacancy-free compositions $Ba_8Ni_3Si_{43}$ and $Ba_8Ni_4Si_{42}$. However, the formation of

dx.doi.org/10.1021/ic2027626 | Inorg. Chem. 2012, 51, 4730–4741

vacancies, which are observed in the crystal structure (see following section) may be favored by entropy contributions.

3.5. Crystal Structure. The clathrate-I structure (space group $Pm\bar{3}n$, No. 223) is represented by two Wyckoff sites for guest atoms (2*a*, 6*d*) and three sites for the atoms in the host framework (6*c*, 16*i*, 24*k*; Figure 6). The framework, which

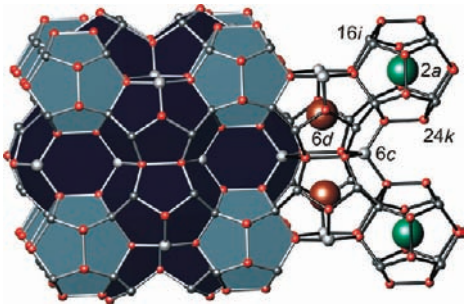

Figure 6. Crystal structure of the type-I clathrate. 20- and 24-atom polyhedra are shown in light and dark blue, respectively. Guest atoms at 2*a* (gray) and 6*d* (brown) as well as atoms (or vacancies) in the host framework at 6*c* (white), 16*i* (green), and 24*k* (red) sites are shown.

consists of four-bonded atoms forming twisted pentagons and planar hexagons, encloses 20-vertex [5^{12}] polyhedra centered by a 2*a* site and 24-vertex [$6^2 5^{12}$] polyhedra centered by a 6d site. The hexagons formed by atoms at 6*c* and 24*k* sites are connected via common 6*c* atoms to infinite chains along ⟨100⟩. Atoms at the 6*c* site join two hexagons with bond angles around 120° making this coordination environment unfavorable especially for four-bonded Si atoms. Hence, vacancies or substitution atoms are preferentially found at this site.

Crystal structure determinations were performed on three single crystals selected from samples annealed at 1000 °C with WDXS compositions $Ba_{8.00(3)}Ni_{2.62(1)}Si_{42.57(3)}$ (**I**), $Ba_{8.00(2)}Ni_{3.17(1)}Si_{43.03(2)}$ (**II**), and $Ba_{8.00(4)}Ni_{3.72(9)}Si_{41.83(5)}$ (**III**) (Table 3, Figure 1b). Structure refinement revealed in all cases full occupancy of Ba1 at 2*a* site and Ba2 at 6*d* site. Ba2 in oversized 24-atom cages shows relatively large anisotropic displacement which is usually interpreted as off-centered positioning of the guest atoms.[38,39] When the Ba2 atoms were refined at the 24*k* site with 0.25 occupancy, the residual values were considerably lowered (e.g., R_F for **I** drops from 3.9 to 3.0%). In the next step, the Ni to Si ratio of the framework site 6*c* was refined assuming full site occupancy, while sites 16*i* and 24*k* were refined with full Si occupancy. With such distribution of Ni and Si, the number of Ni atoms per formula unit was obtained to be 2.49(6) for **I**, 2.90(5) for **II**, and 3.05(4) for **III** which is distinctly lower than the respective Ni content obtained from WDXS analyses. The discrepancy can be explained by the presence of vacancies at the 6*c* site, which was also indicated by the slightly increasing displacement anisotropy of the Si atoms at the 24*k* site. This sizable anisotropy has been correlated with the amount of vacancies as shown for $Cs_8Sn_{44}\square_2$,[40] $K_8Ge_{44}\square_2$,[41] and for ternary variants $Ba_8TM_x\square_yGe_{46-x-y}$ (*TM* = Ni,[42] Pd,[43] Pt,[44] Zn,[45,46] etc.).

In the next step of the structure refinement, the Ni content was fixed according to WDXS analysis. The final structure refinements yielded the compositions $Ba_8Ni_{2.6}Si_{43.3}\square_{0.1}$ for **I**, $Ba_8Ni_{3.2}Si_{42.4}\square_{0.4}$ for **II**, and $Ba_8Ni_{3.7}Si_{41.4}\square_{0.9}$ for **III** (see Tables 1 and 2 and Tables S1–S3 in the Supporting Information). Because of the mixed occupancy of the 6*c* site by vacancies, Ni, and Si, the atoms in the neighboring 24*k* site may be located at three different positions. In particular, the presence of vacancies at the 6*c* site leads to a shift of the neighboring atoms toward the vacancy position. Because of the small amount of vacancies in crystal **I**, position Si33 could not be resolved. The interatomic distances *d*(Si1–Si31) varying in the range 2.40–2.46 Å are slightly longer than the Si–Si distance in α-Si (~2.35 Å), but agree well with those observed for other silicon clathrates, e.g., $Na_2Ba_6Si_{46}$ (*d*(Si1–Si3) ≈ 2.39,[47] 2.40 Å[48]), Ba_8Si_{46} (*d*(Si1–Si3) ≈ 2.42 Å),[5] or $Cs_{7.8}Si_{46}$ (*d*(Si1–Si3) ≈ 2.44 Å).[49] The distances *d*(Ni–Si32) ≈ 2.28–2.33 Å are in the range with those reported in NiSi as *d*(Ni–Si) ≈ 2.29–2.40 Å,[50] or in $NiSi_2$ as *d*(Ni–Si) ≈ 2.34 Å.[33] The shorter distance *d*(Ni–Si) compared to *d*(Si–Si) explains the contraction of the framework with increasing Ni content as revealed by PXRD data (Figure 7). Distances *d*(□–Si33) are

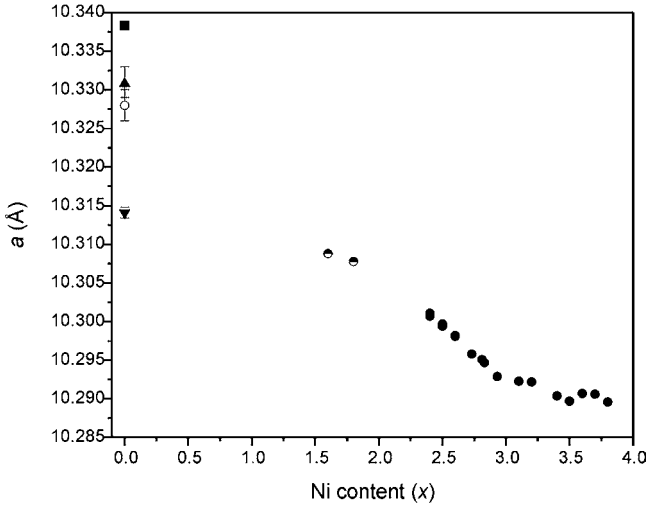

Figure 7. Lattice parameter of Ba_8Si_{46} (○),[5] Ba_8Si_{46} (extrapolated based on our data and $Ba_{8-\delta}Si_{46}$[24]) (■), $Ba_{7.76}Si_{46}$ (▼),[22] $Ba_{7.6}Si_{46}$ (▲),[6] $Ba_{8-\delta}Ni_xSi_{46-x}$ obtained by steel-quenching (◓), and clathrate samples annealed at 1000 °C (●) with respect to determined Ni content. For our samples, the errors of the lattice parameters are smaller than the size of the symbols used.

found to be ~2.15 Å for **II** and ~2.19 Å for **III**. Consequently, the clathrate $Ba_8Ni_x\square_ySi_{46-x-y}$ constitutes a rare example of a Si-based clathrate with framework vacancies. The only other example was $Ba_8Al_{14}Si_{31}\square_1$,[51] although a very similar composition $Ba_8Al_{15}Si_{31}$ was reported later without framework vacancies.[52]

The crystal structure of the phase $Ba_{8-\delta}Ni_xSi_{46-x}$ obtained by steel-quenching (see section 3.3) was refined from PXRD data for samples with nominal $\delta = 0$, $x = 0.2$, and $x = 0.5$. In the structure refinement, the site 2*a* was found to be partially occupied by Ba atoms in both samples. However, Ba2 at 6*d* site, the framework sites Ni1/Si1 at 6*c*, Si2 at 16*i*, and Si3 at 24*k* were refined with full occupancy (see Figure S6 and S7 and Tables S4–S6 in the Supporting Information). Accordingly, the compositions were determined to be $Ba_{7.9(1)}Ni_{1.4(1)}Si_{44.6(1)}$ and $Ba_{7.9(1)}Ni_{1.6(1)}$ $Si_{44.4(1)}$ for the samples prepared with $x = 0.2$ and $x = 0.5$, respectively.

3.6. X-ray Absorption Spectroscopy. It was reported by several studies dealing with Ni compounds (e.g., $KNiIO_6$, $LiNiO_2$, NiO; $LaNiO_3$, $LaNi_2O_5$, $LaNiO_2$) that the energy of the X-ray absorption edge correlates well with Ni valency and

dx.doi.org/10.1021/ic2027626 | Inorg. Chem. 2012, 51, 4730–4741

shifts to higher values as the valency increases.[53,54] X-ray absorption spectra of $Ba_8Ni_x\square_ySi_{46-x-y}$ were determined close to the Ni *K*-edge (8333 eV) on four samples annealed at 700 °C with determined Ni contents x = 2.6, 3.1, 3.4, and 3.8 (Figure 8a). For comparison, the spectra of Ni foil, NiSi, NiI_2,

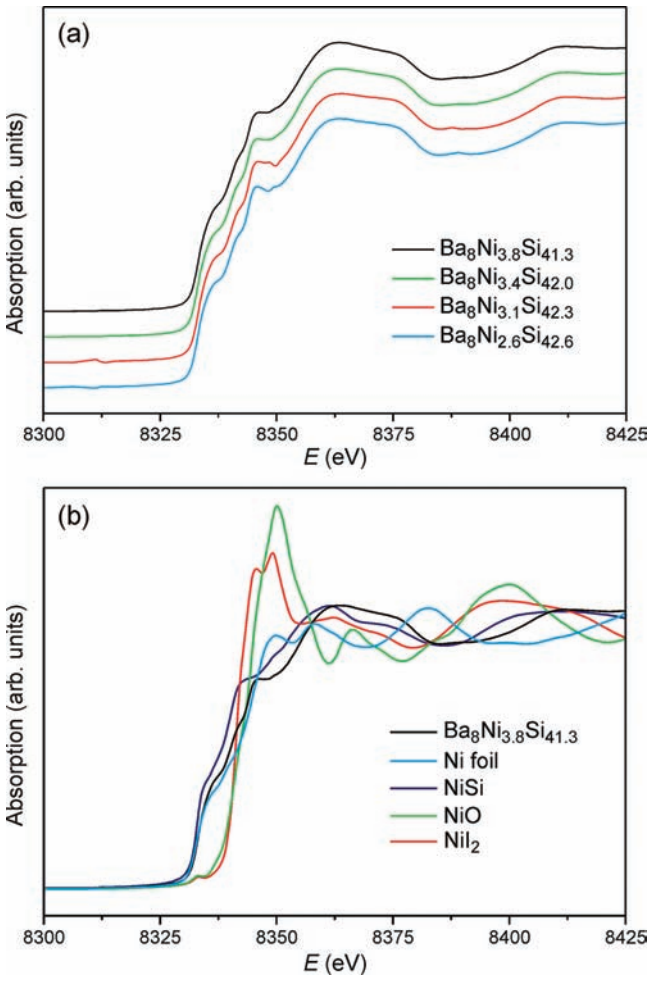

Figure 8. Normalized Ni *K*-edge XANES spectra: (a) The clathrate $Ba_8Ni_x\square_ySi_{46-x-y}$ with determined compositions $Ba_8Ni_{2.6}Si_{42.6}$, $Ba_8Ni_{3.1}Si_{42.3}$, $Ba_8Ni_{3.4}Si_{42}$, and $Ba_8Ni_{3.8}Si_{41.3}$; (b) Ni foil, NiSi, NiO, and NiI_2. Spectra are shifted vertically for clarity.

and NiO were also recorded (Figure 8b). The Ni *K*-edge XANES and EXAFS regions of all clathrate samples show qualitatively identical features. Near the Ni *K*-edge, the spectra exhibit distinct characteristics dominated by the dipole-allowed transition of the Ni-1*s* electron to unoccupied 4*p* states (Figure 8a). The position of the Ni absorption edge was found to be very close to those of Ni foil and NiSi and distinctly separated from those of NiI_2 and NiO. Accordingly, the electronic state of Ni in clathrate $Ba_8Ni_x\square_ySi_{46-x-y}$ is close to that in the element. EXAFS data for all clathrate samples show almost identical features pointing to very similar local environments (Figure 9). The major peak in the Fourier-transformed curves reflects the 4-fold coordination of the Ni atoms by Si atoms with d(Ni−Si) ≈ 2.2 Å. The broad peak at around 3.7 Å is associated to Ni−Ba2 contacts. A related EXAFS analysis was performed on the clathrate-I $Ba_8Cu_4Si_{42}$ revealing that Cu atoms are located at the 6*c* site,[55] which is in agreement with the crystal structure investigations.[8,21,56]

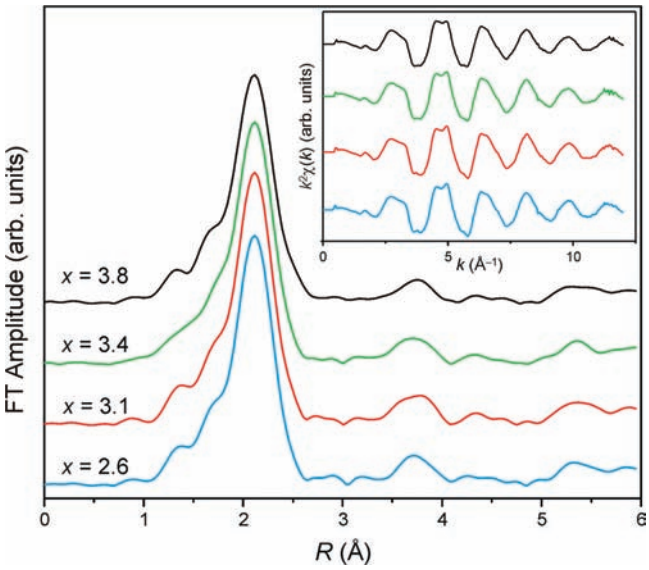

Figure 9. k^2-weighted Ni *K*-edge EXAFS (inset) and associated Fourier transform for the clathrate $Ba_8Ni_x\square_ySi_{46-x-y}$ with determined compositions $Ba_8Ni_{2.6}Si_{42.6}$, $Ba_8Ni_{3.1}Si_{42.3}$, $Ba_8Ni_{3.4}Si_{42}$, and $Ba_8Ni_{3.8}Si_{41.3}$.

3.7. Thermoelectric Properties. In the previous report,[25] the transport properties of $Ba_8Ni_x\square_ySi_{46-x-y}$ were discussed in detail for the temperature range 2−350 K. For all compositions investigated, the clathrate phase shows metallic behavior in which both holes and electrons are involved in the electrical conduction. Herein, the previous work is complemented by the determination of the thermoelectric properties in the temperature range 300−773 K (Figure 10). The electrical resistivity of the samples increases linearly with increasing temperature in agreement with the metallic-like behavior observed in the low temperature range, and reaches the values between 3.5 and 5.9 μΩm at 750 K (Figure 10a). The substitution of Si by Ni results in a slight increase of the electrical resistivity. Regardless of the composition, the thermopower values remain negative above room temperature, indicating a dominant contribution from electrons (Figure 10b). The metallic character of these samples results in moderate values of thermopower that increase in absolute values with temperature reaching the values between −30 and −55 μV K^{-1} at 750 K. A clear trend of the thermopower values as a function of the Ni content was not observed. This behavior can be attributed to a balance between the hole and electron contributions as previously shown in the low-temperature investigation.[25]

For all compositions, the thermal conductivity values are weakly temperature dependent ranging between 4.0 and 6.5 W m^{-1} K^{-1} at 773 K (Figure 10c). The measured values decrease with increasing Ni content up to x = 3.4. The observed behavior against x mainly reflects the variation of the electrical resistivity as evidenced by the temperature dependence of the lattice and electronic thermal conductivity displayed in Figure 10d. To separate these two contributions, the electrical resistivity values were used to estimate the electronic contribution, λ_e, via the Wiedemann−Franz law $\lambda_e = LT/\rho$. The Lorenz number L was assumed as a first approximation to be equal to the value of a degenerate electron gas $L = L_0 = 2.44 \times 10^{-8}$ V^2 K^{-2}. The lattice thermal conductivity values λ_L are in the expected range for Si-based clathrates and decrease with increasing temperature as a result of dominant phonon−

dx.doi.org/10.1021/ic2027626 | Inorg. Chem. 2012, 51, 4730−4741

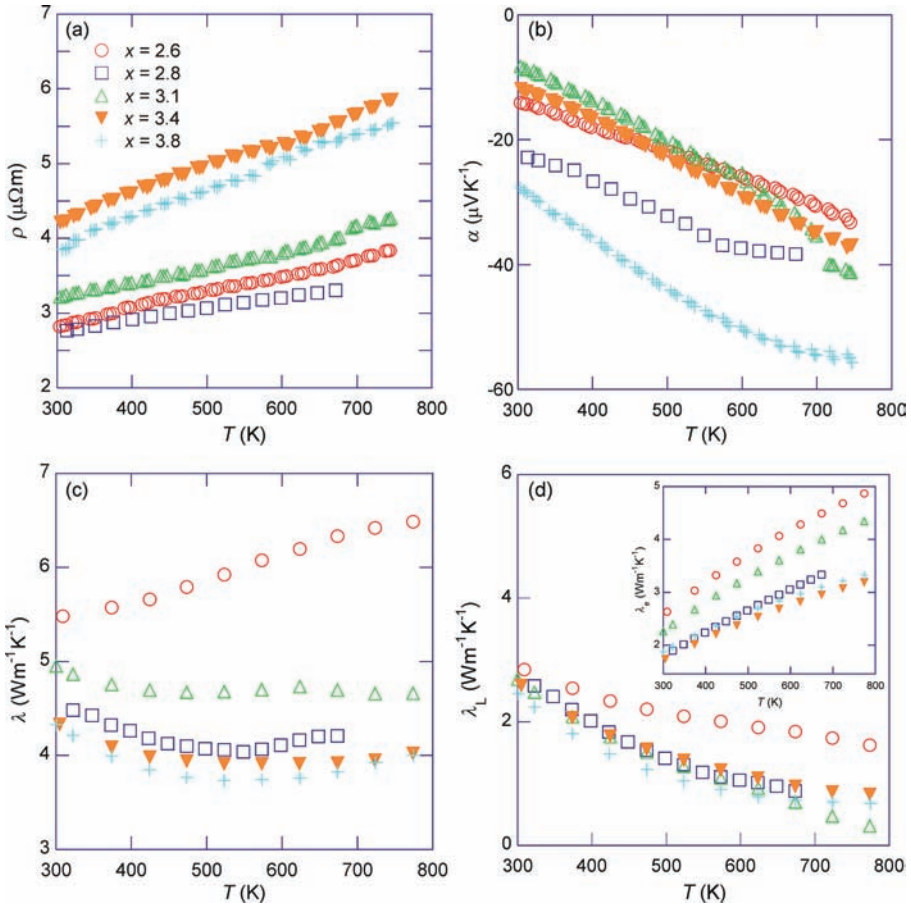

Figure 10. Transport properties of the clathrate $Ba_8Ni_x\square_ySi_{46-x-y}$ with determined compositions $Ba_8Ni_{2.6}Si_{42.6}$ (red circle), $Ba_8Ni_{2.8}Si_{42.1}$ (blue square), $Ba_8Ni_{3.1}Si_{42.3}$ (green triangle), $Ba_8Ni_{3.4}Si_{42}$ (orange triangle), and $Ba_8Ni_{3.8}Si_{41.3}$ (aqua plus sign). Temperature dependence of (a) the electrical resistivity, (b) the thermopower, (c) the total thermal conductivity, and the lattice and (d) electronic thermal conductivities (inset) are shown.

phonon interactions. In addition, λ_L decreases slightly as the Ni concentration increases. The combination of the transport properties results in a maximum ZT value of around 0.1 at 700 K for the sample with x = 3.8. The metallic nature of these samples is the main reason for the low ZT values.

3.8. Superconductivity. Low-temperature electrical resistivity $\rho(T)$ of $Ba_{8-\delta}Ni_xSi_{46-x}$ phase with low Ni content shows superconducting behavior (Figure 11). The ρ values of the samples with compositions $Ba_{7.9(1)}Ni_{1.4(1)}Si_{44.6(1)}$ and $Ba_{7.9(1)}Ni_{1.6(1)}Si_{44.4(1)}$ remained quasi-constant down to the superconducting transition with onsets at T_c = 6 and 5.5 K and zero-resistance temperatures 3.5 and 3 K, respectively. The broad superconducting transitions of $\Delta T_c \sim 2.5$ K for both compounds may be related to inhomogeneities in the Ni content arising from rapid cooling. Since X-ray diffraction measurements together with the EDXS analyses revealed no detectable impurity phases, this indicates that the superconducting transition observed is an intrinsic property of the clathrate phase at these compositions. The presence of Ni results in a slight decrease of T_c compared to Ba_8Si_{46} where a superconducting state sets in at 8 K. Higher Ni contents ($x \geq 2.4$) resulted in a complete suppression of superconductivity down to 0.4 K as shown by low-temperature electrical resistivity measurements.[25] This sharp decrease in T_c with Ni content reflects the evolution of the density of states at the Fermi level, $N(E_F)$, which shows only slight variation for $0 \leq x \leq 2.0$ before exhibiting a drastic decrease between x = 2.0 and x = 3.0.[25]

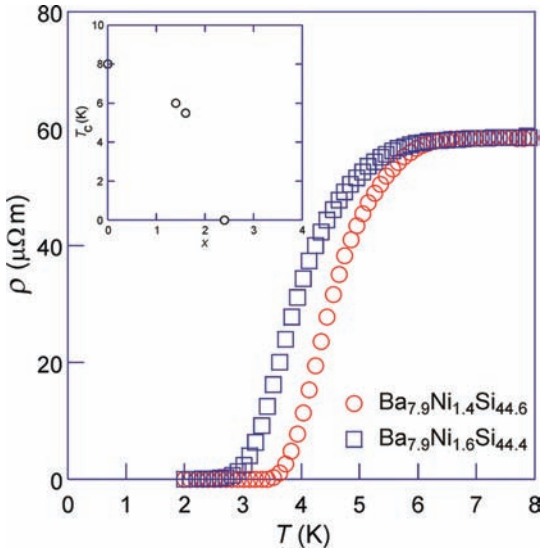

Figure 11. Electrical resistivity of the steel-quenched samples as a function of temperature: $Ba_{7.9(1)}Ni_{1.4(1)}Si_{44.6(1)}$ (red circle) and $Ba_{7.9(1)}Ni_{1.6(1)}Si_{44.4(1)}$ (blue square), showing the superconducting transition with onsets at 6.0 and 5.5 K, respectively. The inset figure illustrates the evolution of the critical temperature T_c as a function of the Ni content. The T_c value of Ba_8Si_{46} ($x \neq 0$) is taken from Yamanaka et al.[5].

dx.doi.org/10.1021/ic2027626 | Inorg. Chem. 2012, 51, 4730–4741

Thus the decrease in the electron−phonon coupling strength in $Ba_{8-\delta}Ni_x\square_ySi_{46-x-y}$ originates from the Ni-content-dependent variations in the electronic band structure.[25] A decrease in T_c is a feature shared by all ternary type-I clathrates investigated so far showing that alloying on either the Ba or Si site tends to suppress superconductivity. However, the variation in T_c strongly depends on the substituting element as found out in several studies on $Ba_8M_xSi_{46-x}$ for M = Ge,[6] Ga,[7] or Cu.[8] Although a superconducting state still develops in the Ge- and Ga-substituted systems up to x = 25 and x = 10, respectively, a lower Cu content of x = 4 is sufficient to drop T_c from 8 K down to 2.9 K. In the present case, Ni has a stronger influence since the superconductivity disappears for $x \geq 2.4$.

4. CONCLUSIONS

The homogeneity range of the clathrate-I phase $Ba_8Ni_x\square_ySi_{46-x-y}$ was determined to be $2.4 \leq x \leq 3.8$ and $0 \leq y \leq 0.9$ at 1000 °C. The experimental result is in agreement with the heat of formation calculations. Reinvestigation of the crystal structure showed that the clathrate-I phase contains framework vacancies increasing in number with Ni content reaching up to $y \approx 0.9$ for x = 3.7. For all compositions, XANES investigations indicate that the electronic state of the Ni atoms is close to that of the element. The electronic transport behavior of all samples exhibits metallic-like behavior with moderate thermopower values at high temperatures. The thermal conductivity values for all compositions are low as in other clathrate phases. A maximum ZT value of around 0.1 was obtained at 700 K for the sample with x = 3.8. The metastable clathrate phase $Ba_{8-\delta}Ni_xSi_{46-x}$ was prepared by steel-quenching and shows superconducting transition with onset temperatures at 6.0 and 5.5 K for x = 1.4 and 1.6, respectively.

■ ASSOCIATED CONTENT

Ⓢ Supporting Information

X-ray crystallographic data in CIF format, X-ray powder patterns, DSC results, SEM images, tables of crystallographic data, atomic coordinates, displacement parameters, site occupancies, and interatomic distances. This material is available free of charge via the Internet at http://pubs.acs.org.

■ AUTHOR INFORMATION

Corresponding Author

*E-mail: aydemir@cpfs.mpg.de; grin@cpfs.mpg.de. Tel.: +49-351-46464000.

Notes

The authors declare no competing financial interest.

■ ACKNOWLEDGMENTS

The authors acknowledge Petra Scheppan, Monika Eckert, Renate Hempel-Weber, and members of the Kompetenzgruppe Struktur for providing experimental support. C.C. acknowledges the financial support of the CNRS-MPG program. M.B. and Y.G. gratefully acknowledge financial support by the Deutsche Forschungsgemeinschaft (SPP 1415, "Kristalline Nichtgleichgewichtsphasen (KNG) - Präparation, Charakterisierung und in situ-Untersuchung der Bildungsmechanismen").

■ REFERENCES

(1) Kasper, J. S.; Hagenmuller, P.; Pouchard, M.; Cros, C. *Science* **1965**, *150*, 1713−1714.
(2) Stefanoski, S.; Martin, J.; Nolas, G. S. *J. Phys.: Condens. Matter* **2010**, *22*, 485404.
(3) Yamanaka, S.; Horie, H.; Nakano, H.; Ishikawa, M. *Fullerene Sci. Technol.* **1995**, *3*, 21−28.
(4) Kawaji, H.; Horie, H.; Yamanaka, S.; Ishikawa, M. *Phys. Rev. Lett.* **1995**, *74*, 1427−1429.
(5) Yamanaka, S.; Enishi, E.; Fukuoka, H.; Yasukawa, M. *Inorg. Chem.* **2000**, *39*, 56−58.
(6) Fukuoka, H.; Kiyoto, J.; Yamanaka, S. *J. Solid State Chem.* **2003**, *175*, 237−244.
(7) Li, Y.; Zhang, R. H.; Liu, Y.; Chen, N.; Luo, Z. P.; Ma, X. Q.; Cao, G. H.; Feng, Z. S.; Hu, C. R.; Ross, J. H. *Phys. Rev. B* **2007**, *75*, 054513.
(8) Li, Y.; Liu, Y.; Chen, N.; Cao, G. H.; Feng, Z. S.; Ross, J. H. *Phys. Lett. A* **2005**, *345*, 398−408.
(9) Kamakura, N.; Nakano, T.; Ikemoto, Y.; Usuda, M.; Fukuoka, H.; Yamanaka, S.; Shin, S.; Kobayashi, K. *Phys. Rev. B* **2005**, *72*, 014511.
(10) Kuznetsov, V. L.; Kuznetsova, L. A.; Kaliazin, A. E.; Rowe, D. M. *J. Appl. Phys.* **2000**, *87*, 7871−7875.
(11) Bentien, A.; Nishibori, E.; Paschen, S.; Iversen, B. B. *Phys. Rev. B* **2005**, *71*, 144107.
(12) Blake, N. P.; Bryan, D.; Latturner, S.; Mollnitz, L.; Stucky, G. D.; Metiu, H. *J. Chem. Phys.* **2001**, *114*, 10063−10074.
(13) Kleinke, H. *Chem. Mater.* **2010**, *22*, 604−611.
(14) Nolas, G. S.; Slack, G. A.; Schujman, S. B., Semiconductor clathrates: A phonon glass electron crystal material with potential for thermoelectric applications. In *Semiconductors and Semimetals*; Terry, M. T., Ed.; Elsevier: Amsterdam, 2001; Vol. *69*, Chapter 6, pp 255−300.
(15) Rowe, D. M. *CRC Handbook of Thermoelectrics*; CRC Press: Boca Raton, FL, 1995.
(16) Snyder, G. J.; Toberer, E. S. *Nat. Mater.* **2008**, *7*, 105−114.
(17) Johnsen, S.; Bentien, A.; Madsen, G. K. H.; Nygren, M.; Iversen, B. B. *Phys. Rev. B* **2007**, *76*, 245126.
(18) Bentien, A.; Johnsen, S.; Iversen, B. B. *Phys. Rev. B* **2006**, *73*, 094301.
(19) Jaussaud, N.; Gravereau, P.; Pechev, S.; Chevalier, B.; Ménétrier, M.; Dordor, P.; Decourt, R.; Goglio, G.; Cros, C.; Pouchard, M. *C. R. Chim.* **2005**, *8*, 39−46.
(20) Aydemir, U.; Candolfi, C.; Ormeci, A.; Oztan, Y.; Baitinger, M.; Oeschler, N.; Steglich, F.; Grin, Yu. *Phys. Rev. B* **2011**, *84*, 195137.
(21) Cordier, G.; Woll, P. *J. Less Common Met.* **1991**, *169*, 291−302.
(22) Fukuoka, H.; Kiyoto, J.; Yamanaka, S. *Inorg. Chem.* **2003**, *42*, 2933−2937.
(23) Toulemonde, P.; Adessi, C.; Blase, X.; San Miguel, A.; Tholence, J. L. *Phys. Rev. B* **2005**, *71*, 094504.
(24) Liang, Y.; Böhme, B.; Reibold, M.; Schnelle, W.; Schwarz, U.; Baitinger, M.; Lichte, H.; Grin, Yu. *Inorg. Chem.* **2011**, *50*, 4523−4528.
(25) Candolfi, C.; Aydemir, U.; Ormeci, A.; Baitinger, M.; Oeschler, N.; Steglich, F.; Grin, Yu. *Phys. Rev. B* **2011**, *83*, 205102.
(26) Aydemir, U.; Candolfi, C.; Borrmann, H.; Baitinger, M.; Ormeci, A.; Carrillo-Cabrera, W.; Chubilleau, C.; Lenoir, B.; Dauscher, A.; Oeschler, N.; Steglich, F.; Grin, Yu. *Dalton Trans.* **2010**, *39*, 1078−1088.
(27) Akselrud, L. G.; Zavalii, P. Y.; Grin, Yu.; Pecharsky, V. K.; Baumgartner, B.; Wölfel, E. *Mater. Sci. Forum* **1993**, *335*, 133−136.
(28) Koepernik, K.; Eschrig, H. *Phys. Rev. B* **1999**, *59*, 1743−1757.
(29) Perdew, J. P.; Wang, Y. *Phys. Rev. B* **1992**, *45*, 13244−13249.
(30) Kittel, C., *Introduction to Solid State Physics*, 7th ed.; Wiley: New York, 1996; p 23.
(31) Goebel, T.; Prots, Y.; Haarmann, F. *Z. Kristallogr. NCS* **2009**, *224*, 7−8.
(32) Rabadanov, M. K.; Ataev, M. B. *Crystallogr. Rep.* **2002**, *47*, 33−38.
(33) Ackerbauer, S.; Krendelsberger, N.; Weitzer, F.; Hiebl, K.; Schuster, J. C. *Intermetallics* **2009**, *17*, 414−420.
(34) Massalski, T. B., *Binary Alloy Phase Diagram*, 2nd ed.; ASM International: Materials Park, OH, 1990; pp 613−615.
(35) Massalski, T. B. *Binary Alloy Phase Diagrams*. 2nd ed.; ASM International: Materials Park, OH, 1990; pp 2859−2861.

(36) Imai, Y.; Watanabe, A. *Intermetallics* **2010**, *18*, 542−547.
(37) Iitaka, T. *Phys. Rev. B* **2007**, *75*, 012106.
(38) Pauling, L.; Marsh, R. E. *Proc. Natl. Acad. Sci. U.S.A.* **1952**, *38*, 112−118.
(39) Baumbach, R.; Bridges, F.; Downward, L.; Cao, D.; Chesler, P.; Sales, B. *Phys. Rev. B* **2005**, *71*, 024202.
(40) von Schnering, H. G.; Kroner, R.; Baitinger, M.; Peters, K.; Nesper, R.; Grin, Yu. *Z. Kristallogr. NCS* **2000**, *215*, 205−206.
(41) von Schnering, H. G.; Llanos, J.; Peters, K.; Baitinger, M.; Grin, Yu.; Nesper, R. *Z. Kristallogr. NCS* **2011**, *226*, 9−10.
(42) Nguyen, L. T. K.; Aydemir, U.; Baitinger, M.; Bauer, E.; Borrmann, H.; Burkhardt, U.; Custers, J.; Haghighirad, A.; Hofler, R.; Luther, K. D.; Ritter, F.; Assmus, W.; Grin, Yu.; Paschen, S. *Dalton Trans.* **2010**, *39*, 1071−1077.
(43) Melnychenko-Koblyuk, N.; Grytsiv, A.; Rogl, P.; Rotter, M.; Bauer, E.; Durand, G.; Kaldarar, H.; Lackner, R.; Michor, H.; Royanian, E.; Koza, M.; Giester, G. *Phys. Rev. B* **2007**, *76*, 144118.
(44) Melnychenko-Koblyuk, N.; Grytsiv, A.; Rogl, P.; Rotter, M.; Lackner, R.; Bauer, E.; Fornasari, L.; Marabelli, F.; Giester, G. *Phys. Rev. B* **2007**, *76*, 195124.
(45) Melnychenko-Koblyuk, N.; Grytsiv, A.; Fornasari, L.; Kaldarar, H.; Michor, H.; Rohrbacher, F.; Koza, M.; Royanian, E.; Bauer, E.; Rogl, P.; Rotter, M.; Schmid, H.; Marabelli, F.; Devishvili, A.; Doerr, M.; Giester, G. *J. Phys.: Condens. Matter* **2007**, *19*, 216223.
(46) Alleno, E.; Maillet, G.; Rouleau, O.; Leroy, E.; Godart, C.; Carrillo-Cabrera, W.; Simon, P.; Grin, Yu. *Chem. Mater.* **2009**, *21*, 1485−1493.
(47) Böhme, B.; Aydemir, U.; Ormeci, A.; Schnelle, W.; Baitinger, M.; Grin, Yu. *Sci. Technol. Adv. Mat.* **2007**, *8*, 410−415.
(48) Baitinger, M.; von Schnering, H. G.; Chang, J. H.; Peters, K.; Grin, Yu. *Z. Kristallogr. NCS* **2007**, *222*, 87−88.
(49) Wosylus, A.; Veremchuk, I.; Schnelle, W.; Baitinger, M.; Schwarz, U.; Grin, Y. *Chem.—Eur. J.* **2009**, *15*, 5901−5903.
(50) Wopersnow, W.; Schubert, K. *Z. Metallkd.* **1976**, *67*, 807−810.
(51) Condron, C. L.; Martin, J.; Nolas, G. S.; Piccoli, P. M. B.; Schultz, A. J.; Kauzlarich, S. M. *Inorg. Chem.* **2006**, *45*, 9381−9386.
(52) Tsujii, N.; Roudebush, J. H.; Zevalkink, A.; Cox-Uvarov, C. A.; Snyder, G. J.; Kauzlarich, S. M. *J. Solid State Chem.* **2011**, *184*, 1293−1303.
(53) Mansour, A. N.; Melendres, C. A. *J. Phys. Chem. A* **1998**, *102*, 65−81.
(54) Crespin, M.; Levitz, P.; Gatineau, L. *J. Chem. Soc., Faraday Trans. 2* **1983**, *79*, 1181−1194.
(55) Yang, L.; Wang, Y.; Liu, T.; Hu, T. D.; Li, B. X.; Ståhl, K.; Chen, S. Y.; Li, M. Y.; Shen, P.; Lu, G. L.; Wang, Y. W.; Jiang, J. Z. *J. Solid State Chem.* **2005**, *178*, 1773−1777.
(56) Yan, X.; Giester, G.; Bauer, E.; Rogl, P.; Paschen, S. *J. Electron. Mater.* **2010**, *39*, 1634−1639.